



# Peculiar synergistic effect of MoS<sub>2</sub> quantum dots and graphene on Metal-Organic Frameworks for photocatalytic hydrogen evolution

Xuqiang Hao <sup>a,c</sup>, Zhiliang Jin <sup>a,\*</sup>, Hao Yang <sup>a</sup>, Gongxuan Lu <sup>b</sup>, Yingpu Bi <sup>b</sup>

<sup>a</sup> School of Chemistry and Chemical Engineering, Beifang University of Nationalities, Yinchuan 750021, PR China

<sup>b</sup> State Key Laboratory for Oxo Synthesis and Selective Oxidation, Lanzhou Institute of Chemical Physics, Chinese Academy of Science, Lanzhou 730000, PR China

<sup>c</sup> School of Chemistry and Chemical Engineering, Nanjing University, Nanjing 210023, PR China



## ARTICLE INFO

### Article history:

Received 4 January 2017

Received in revised form 4 March 2017

Accepted 19 March 2017

Available online 23 March 2017

### Keywords:

MoS<sub>2</sub> QDs

Metal-organic frameworks

Graphene

Photocatalytic hydrogen evolution

## ABSTRACT

Special enhanced synergistic effect of MoS<sub>2</sub> quantum dots (MoS<sub>2</sub> QDs) and graphene on metal-organic frameworks for photocatalytic hydrogen evolution is obtained here. The photocatalytic activity of H<sub>2</sub> evolution reach 186.37 μmol over the EY-sensitized 5 wt% MoS<sub>2</sub> QDs/UiO-66-NH<sub>2</sub>/G irradiated under visible light irradiation ( $\lambda \geq 420$  nm) in the first 3 h, and the apparent quantum efficiency (AQE) is 40.5% at 430 nm. The synergistic effect between MoS<sub>2</sub> QDs and graphene together with UiO-66-NH<sub>2</sub> is corroborated by photo-luminescence spectra, electro-chemical and photo-electro-chemical experiments. It demonstrate that the charge separation and the electrons transfer are more efficient with the aid of the MoS<sub>2</sub> QDs and graphene. MoS<sub>2</sub> QDs might be a potential photocatalyst for design new type of catalysts in photocatalysis proton reduction.

© 2017 Elsevier B.V. All rights reserved.

## 1. Introduction

With a view to the growing concerns about global energy crisis and environmental issues, considerable efforts have been invested in clean energy sources to replace exhaustible fossil fuels. Hydrogen, with the fuel value ( $\sim 143$  kJ g<sup>-1</sup>) three times higher than gasoline and only non-polluted water as by-product, is a possible candidate for future energy supplies [1–3]. Among various strategies for hydrogen evolution, the photocatalysis is considered as a most promising way, because it can direct utilization of solar energy to achieve H<sub>2</sub> generation from water splitting, as well as its potentially enables much simpler and more economically competitive systems [4]. Numerous efforts have carried out to develop efficient photocatalytic systems and photocatalysts over the past decades. However, up to now, the high cost noble metals noble metals remain dominantly as the most efficient co-catalysts [5]. Therefore, to develop low-cost non-noble-metal co-catalysts become an urgent task for advancing photocatalytic H<sub>2</sub> production.

Recently, the transition-metal dichalcogenide semiconductor molybdenum disulfide (MoS<sub>2</sub>) has been regarded as a promising substitute for noble-metal co-catalysts in photocatalysis reactions [6–9]. The S-Mo-S coordination in the crystal lattices generates

unsaturated Mo and S atoms at the edge, leading to the unique “edges activity” of MoS<sub>2</sub> [2]. However, the limitation of active edges and the specific surface of MoS<sub>2</sub> have hindered the catalytic activity of MoS<sub>2</sub>-based catalysts for efficient hydrogen evolution [2]. Therefore, MoS<sub>2</sub> had been fabricated into different structures to achieve higher catalytic activity for hydrogen evolution, such as nanoparticles, nanosheets, and monolayer or few layers. Among them, the higher quantum confinement and small-size effect of MoS<sub>2</sub> quantum dots (MoS<sub>2</sub> QDs) leads to unsaturated bond on surface and edges, proving more opportunity to connect with other atoms and obtain higher activity toward hydrogen evolution [1,2,10,11]. It is reported that MoS<sub>2</sub> QDs/Graphene/TiO<sub>2</sub> composite photocatalyst was fabricate by a simple one-pot solvothermal approach significant improved photocatalytic activity, which is caused by the increased charge separation, visible-light absorbance, specific surface area and reaction sites upon the introduction of MoS<sub>2</sub> QDs [12]. Others reported that MoS<sub>2</sub>/WS<sub>2</sub> quantum dots rendered good HER catalytic activity, showing a small onset overpotential, along with long-term durability, because its larger concentration of active sites resulting from the unique monolayer and defect-rich nanostructures [13]. Recently, the monolayer MoS<sub>2</sub> QDs improved HER catalytic activities with a low overpotential of approximately 120 mV and a relatively small Tafel slope, owing its ultrathin structure and the abundance of exposed active edge sites, as well as the excellent intrinsic conductivity [14,15]. Moreover, MoS<sub>2</sub> QDs can gather the photoinduced electron around the edges and efficiently

\* Corresponding author.

E-mail addresses: [zl-jin@nun.edu.cn](mailto:zl-jin@nun.edu.cn), [66123466@163.com](mailto:66123466@163.com) (Z. Jin).

prevent charge recombination [2]. Therefore,  $\text{MoS}_2$  QDs is a promising substitute for noble-metal co-catalysts toward photocatalytic hydrogen evolution.

Metal–organic frameworks (MOFs) are a class of crystalline micro-mesoporous hybrid materials that are composed of clusters of a few metallic atoms held in a three-dimensional structure by organic linkers which have shown a variety of potential applications [16]. Especially, MOFs are attracting considerable attention as heterogeneous catalysts by introducing different types of catalytic sites into a porous MOF matrix over the past decade [17–19]. Recently, the utilization of MOFs for solar energy harvesting has been demonstrated, and MOFs are emerged as a new type of promising photocatalysts for water oxidation [17], photocatalytic  $\text{CO}_2$  reduction [18,19], visible-light-driven photocatalytic organic reaction [16] and photocatalytic  $\text{H}_2$  evolution [21]. Compared with the conventional photocatalysts, photoactive MOFs exhibited the highly porous structure with larger surface area, which facilitates the mass transport in photocatalytic reactions [22]. Under light illumination, organic linkers as photon antennas will be excited to generate electrons and holes, which is the essential process for photocatalytic reactions. Moreover, the controllable chemical and physical properties could be easily realized by tuning the organic functionalities and metal center at the molecular level [23]. Garcia and co-workers used a water stable Zr-containing MOFs of  $\text{UiO-66}$  and  $\text{UiO-66(NH}_2\text{)}$  as a photocatalyst for water splitting under UV light irradiation, which opened the door for MOFs to photocatalytic hydrogen evolution from water splitting [21]. However, the MOFs suffered from poor photoactivity, because they cannot respond to visible-light effectively. To extend the photo-response and photoactivity of MOFs, Pt nanoparticles or organometallic compounds have been incorporated into the MOFs to build catalytic-active-sites for hydrogen evolution. For example, Fateeva et al. reported a visible-light-response porphyrin-based MOFs photocatalyst for photocatalytic hydrogen production, which can be attributed to the porphyrins that are versatile functional molecules in catalysis, light harvesting, and molecular sensing [24]. Very Recently, the  $\text{MoS}_2$  and  $\text{CdS}$  nanoparticles decorated on MOFs enhanced photocatalytic activity for hydrogen production under visible light irradiation [25,26]. Dye-sensitization has become a relatively mature technology in solar dye sensitized solar cell for visible-light harvesting and also applied in photocatalysis. The photocatalytic activity of for hydrogen evolution of  $\text{UiO-66(Zr)}$  were extremely enhanced by means of sensitization with Rhodamine B dye [27]. Most recently, the Erythrosin B dye to sensitize Zr-containing MOFs of  $\text{UiO-66}$  also exhibits highly photocatalytic activity for  $\text{H}_2$  production [23]. Both MOFs and dyes containing benzene ring, it is expected that a strong  $\pi$ - $\pi$  stacking and Van Der Waals interaction between MOFs and dyes, which is very important for efficient electron transfer in dye-sensitized photocatalytic system [23]. In addition, the metal centers separated by organic linkers in MOFs can serve as “quantum dots”, therefore the short transport length of charge carriers can be achieved in MOFs. What's more, water molecules can easily diffuse into the pores of MOFs, thus making proton  $\text{H}$  reduction in MOFs as “quasi-homogeneous reaction” [23]. The above-mentioned advantages make dye-sensitized MOFs as potential active photocatalysts for hydrogen production from water reduction.

Graphene was a well-known co-catalyst for efficient photocatalytic  $\text{H}_2$  evolution due to its high specific surface area and superior electron mobility [28]. In this work, metal–organic frameworks  $\text{UiO-66-NH}_2$  grown on graphene ( $\text{UiO-66-NH}_2/\text{G}$ ) by *in situ* solvothermal was employed as a photocatalyst decorating  $\text{MoS}_2$  QDs ( $\text{MoS}_2$  QDs/ $\text{UiO-66-NH}_2/\text{G}$ ) for efficient photocatalytic hydrogen production.  $\text{MoS}_2$  QDs and graphene as dual co-catalysts with the strong light harvesting of EY-sensitized  $\text{UiO-66-NH}_2$  and efficient electron extraction effect of graphene, can efficiently produce  $\text{H}_2$  from water splitting.  $\text{MoS}_2$  QDs with small size exhibit stronger

quantum confinement, higher specific surface area and more edge atoms, resulting in a lack of coordination of the surface atoms and increase in unsaturated bonds [1]. Therefore, these unstable atoms have high surface activity and it is easy to combine with other atoms. Meanwhile, this surface effect offers unique electrical/optical properties, which in favor of the catalytic activity for hydrogen evolution [1]. Moreover, a high apparent quantum yields (AQEs) of 40.5% at 430 nm and a robust photocatalytic activity for  $\text{H}_2$  evolution under visible light irradiation were achieved. Additionally,  $\text{MoS}_2$  QDs/ $\text{UiO-66-NH}_2/\text{G}$  exhibited a better stability for hydrogen production under constant illumination. Interestingly, it was found that the combination of  $\text{MoS}_2$  QDs and graphene together with  $\text{UiO-66-NH}_2$  offered synergistic effects that lead to special reaction pathways which was not seen in  $\text{MoS}_2$  QDs or graphene alone.

## 2. Experimental section

### 2.1. Preparation of photocatalysts

All reagents were analytical grade and used without further purification.

#### 2.1.1. Synthesis of graphene oxide

Graphene oxide (G) was synthesized *via* the same procedure as our previous work [29]. All the reagents were of analytical grade and were used without further purification. In short, 20 g of graphite powder and 10 g of  $\text{NaNO}_3$  were mixed together, followed the mixture was added to cold concentrated  $\text{H}_2\text{SO}_4$  (0 °C, 460 mL) under constant stirring. After 1 h, 60 g of  $\text{KMnO}_4$  was gradually added to the above solution while keeping the temperature less than 20 °C to prevent overheating and explosion. The mixture was then stirred at 35 °C for 2 h and the resulting solution was diluted with 920 mL of water under vigorous stirring for 15 min. The reaction was terminated by adding distilled water (2.8 L) and then  $\text{H}_2\text{O}_2$  solution (50 mL, 30%). The product was filtered, washed repeatedly with  $\text{HCl}$  solution (1:10, v/v) until sulfate could not be detected with  $\text{BaCl}_2$ , and then dried in a vacuum oven at 40 °C for 24 h.

#### 2.1.2. Synthesis of $\text{UiO-66-NH}_2$

$\text{UiO-66-NH}_2$  was synthesized *via* solvothermal route [30]. In a typical synthesis,  $\text{ZrCl}_4$  (0.2332 g, 1.0 mmol) and 2-NH<sub>2</sub>-benzenedicarboxylate (0.1812 g, 1.0 mmol) were dissolved in 50 mL N,N-Dimethylformamide (DMF), and then the solution was transferred to a 100 mL Teflon-lined stainless steel autoclave. The autoclave was sealed and heated in an oven at 120 °C for 48 h. After cooled naturally, the product was collected by centrifugation and washed for three times with DMF, and then sequentially purified within methanol for several times to make sure that the occluded DMF molecules were eliminated, followed by drying under vacuum (100 °C 12 h) before using the samples for the photocatalytic reactions.

#### 2.1.3. Synthesis of $\text{UiO-66-NH}_2/\text{G}$

The synthesis route of  $\text{UiO-66-NH}_2/\text{G}$  was similar to  $\text{UiO-66-NH}_2$ . Typically, 10 mg GO was dispersed in 50 mL DMF by ultrasonication to form a homogeneous solution.  $\text{ZrCl}_4$  (0.2332 g, 1.0 mmol) and 2-NH<sub>2</sub>-benzenedicarboxylate (0.1812 g, 1.0 mmol) were dissolved in the homogeneous solution. After magnetic stirring for 30 min, the solution was transferred to a 100 mL Teflon-lined stainless steel autoclave, and allowed to react following the same steps as mentioned above.

#### 2.1.4. Synthesis of $\text{MoS}_2$ QDs

$\text{MoS}_2$  QDs was synthesized by a surfactant-assisted ultrasonic exfoliated bulk  $\text{MoS}_2$  [1,31]. Typically, 400 mg bulk  $\text{MoS}_2$  powder

was dispersed in 20 mL of N-methylpyrrolidone (NMP) to form a black solution, followed by ultrasonication for three hours at a power of 300 W in an ice-bath. After that, 0.05 M sodium hydroxide (NaOH) was added into solution followed by ultrasonication for another two hours in ice-bath. Then, the solution was first centrifuged at 7000 rpm for 30 min. The supernatant was filtered several times using a 0.22  $\mu$ m organic microporous membrane. The filtrate was added to hexane and chloroform (NMP: hexane: chloroform = 1:1, v/v/v), and the product was collected by centrifugation at 8000 rpm for 10 min [31]. And then the product was dispersed in deionized water (the concentration is 3 mg/mL) for further used.

### 2.1.5. Characterization

The X-ray diffraction (XRD) patterns of the samples were recorded on a Rigaku B/Max-RB diffractometer with a nickel filtrated Cu K $\alpha$  radiation operated at 40 kV and 30 mA. Field emission scanning electron microscopy (FESEM) images were recorded on a JSM-6701F scanning electron microscope operated at an accelerating voltage of 5.0 kV. Transmission electron microscopy (TEM) and high-resolution TEM (HRTEM) images were taken with a Tecnai-G2-F30 field emission transmission electron microscope operating at an accelerating voltage of 300 kV. X-ray photoelectron spectroscopy (XPS) measurements were performed on K-Alpha-surface Analysis (Thermon Scientific) using X-ray monochromatization. The nitrogen adsorption–desorption isotherms of samples were measured at 77 K with an ASAP 2020 M instrument and analyzed by the Brunauer–Emmett–Teller (BET) equation. The pore size distribution plots were obtained by the Barret–Joyner–Halenda (BJH) model. UV/Vis absorption spectra were taken at room temperature on a UV-2550 (Shimadzu) spectrometer. Photoluminescence data (PL) were acquired using a FLUOROMAX-4 spectrophotometer at room temperature.

### 2.1.6. Photocatalytic H<sub>2</sub> evolution experiments

Photocatalytic experiments were conducted in a one-compartment Pyrex reactor *ca.* 178 cm<sup>3</sup> having a flat window *ca.* 10.2 cm<sup>2</sup> for illumination. In a typical photocatalytic experiment, 30 mg of catalyst was suspended in 100 mL 10% (v/v) triethanolamine (TEOA) aqueous solution contain a certain amount of MoS<sub>2</sub> QDs and 28 mg dye Eosin Y (EY) ( $4 \times 10^{-4}$  M) by means of ultrasonication for about 10 min. The opening of the reactor was sealed with a silicone rubber septum. The reactant mixture was degassed by bubbling N<sub>2</sub> gas for 40 min to remove air and ensure that the reaction system was under anaerobic conditions, and then was irradiated by a 300-W Xe lamp with a cutoff filter of 420 nm for H<sub>2</sub> evolution under magnetic stirring condition. The amount of hydrogen evolution was measured using gas chromatography (Tianmei GC7900, TCD, 13X column, N<sub>2</sub> as carrier).

The apparent quantum efficiency (AQE) was measured under the same photocatalytic reaction conditions with irradiation light through a bandpass filter (430, 460, 490, 520, or 550 nm) [32]. Photon flux of the incident light was determined using a Ray virtual radiation actinometer (FU 100, silicon ray detector, light spectrum, 400–700 nm; sensitivity, 10–50  $\mu$ V  $\mu$ mmol<sup>-1</sup> m<sup>-2</sup> s<sup>-1</sup>). The reaction solutions were irradiated for 30 min with bandpass filters for AQE tests on the H<sub>2</sub> production. The following equation was used to calculate the AQE.

$$AQE = \frac{2 \times \text{the number of evolved hydrogen molecules}}{\text{the number of incident photons}} \times 100\% \quad (1)$$

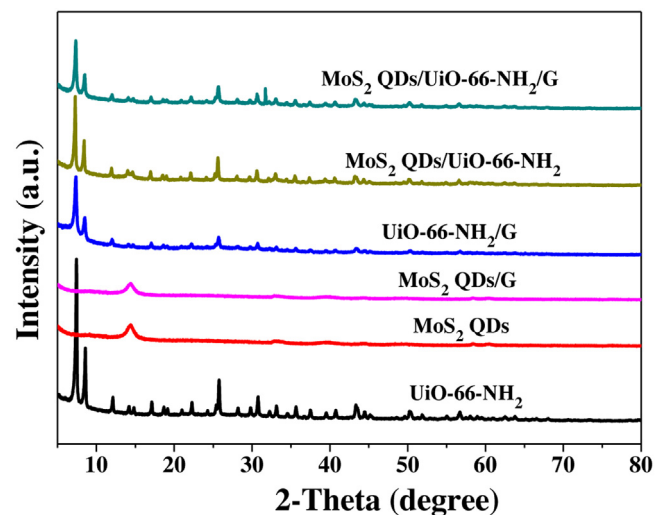


**Fig. 1.** XRD patterns of UiO-66-NH<sub>2</sub>, MoS<sub>2</sub> QDs, MoS<sub>2</sub> QDs/G, UiO-66-NH<sub>2</sub>/G, MoS<sub>2</sub> QDs/UiO-66-NH<sub>2</sub> and MoS<sub>2</sub> QDs/UiO-66-NH<sub>2</sub>/G composites.

The turnover number (TON) and turnover frequency (TOF) of dye Eosin Y for H<sub>2</sub> evolution are calculated by using the following equations [33]:

$$TON = \frac{2 \times \text{number of evolved hydrogen molecules}}{\text{number of dye Eosin Y molecules}} \quad (2)$$

### 2.1.7. Photoelectrochemical measurements

The photoelectrochemical measurement was performed on an electrochemical analyzer (Chenhua CHI 660D) in a standard three-electrode cell [29]. The working electrodes were prepared by drop-coating homogeneous catalyst suspensions directly onto the precleaned indium tin oxide glass (FTO glass) surfaces (1  $\times$  2 cm), and then 500  $\mu$ L of EY aqueous solution ( $4.0 \times 10^{-4}$  mol L<sup>-1</sup>) was added onto the above catalyst film electrode surface and then dried at 100 °C for 1 h. Platinum wire was used as the counter electrode, and a saturated calomel electrode (SCE) as the reference electrode. The supporting electrolyte was 10 v/v% TEOA (pH 7) mixed with 0.1 mol L<sup>-1</sup> Na<sub>2</sub>SO<sub>4</sub> aqueous solution. The surface area of the working electrode exposed to the electrolyte was about 0.95 cm<sup>2</sup>. A 300-W Xe lamp equipped with an optical cutoff filter of 420 nm was employed for the visible-light excitation. EIS Nyquist plots were collected at opencircuit potential, with the frequency ranging from 100 kHz to 0.01 Hz and the modulation amplitude of 5 mV.

## 3. Results and discussion

### 3.1. Characterization supports of catalysts

#### 3.1.1. XRD analysis

Fig. 1 shows the XRD patterns of the UiO-66-NH<sub>2</sub>, MoS<sub>2</sub> QDs, MoS<sub>2</sub> QDs/G, UiO-66-NH<sub>2</sub>/G, MoS<sub>2</sub> QDs/UiO-66-NH<sub>2</sub> and MoS<sub>2</sub> QDs/UiO-66-NH<sub>2</sub>/G nanocomposites to certify the phase structure. It can be seen that the as-prepared UiO-66-NH<sub>2</sub>, UiO-66-NH<sub>2</sub>/G, MoS<sub>2</sub> QDs/UiO-66-NH<sub>2</sub> and MoS<sub>2</sub> QDs/UiO-66-NH<sub>2</sub>/G nanocomposites have the similar XRD patterns. No obvious shift in the peaks of UiO-66-NH<sub>2</sub> is obvious in the UiO-66-NH<sub>2</sub>/G, MoS<sub>2</sub> QDs/UiO-66-NH<sub>2</sub> and MoS<sub>2</sub> QDs/UiO-66-NH<sub>2</sub>/G samples, suggesting that integrity of UiO-66-NH<sub>2</sub> is maintained which not is influenced by graphene and MoS<sub>2</sub> QDs. The sharp peaks of UiO-66-NH<sub>2</sub> indicate its excellent crystallinity, and all the peak can well matched with the reported results [19,30]. MoS<sub>2</sub> QDs and MoS<sub>2</sub> QDs/G samples also have the similar XRD patterns, one small peak at 14.37° belong to (002) plane which fit well with MoS<sub>2</sub> (JCPDS# 77-1716)

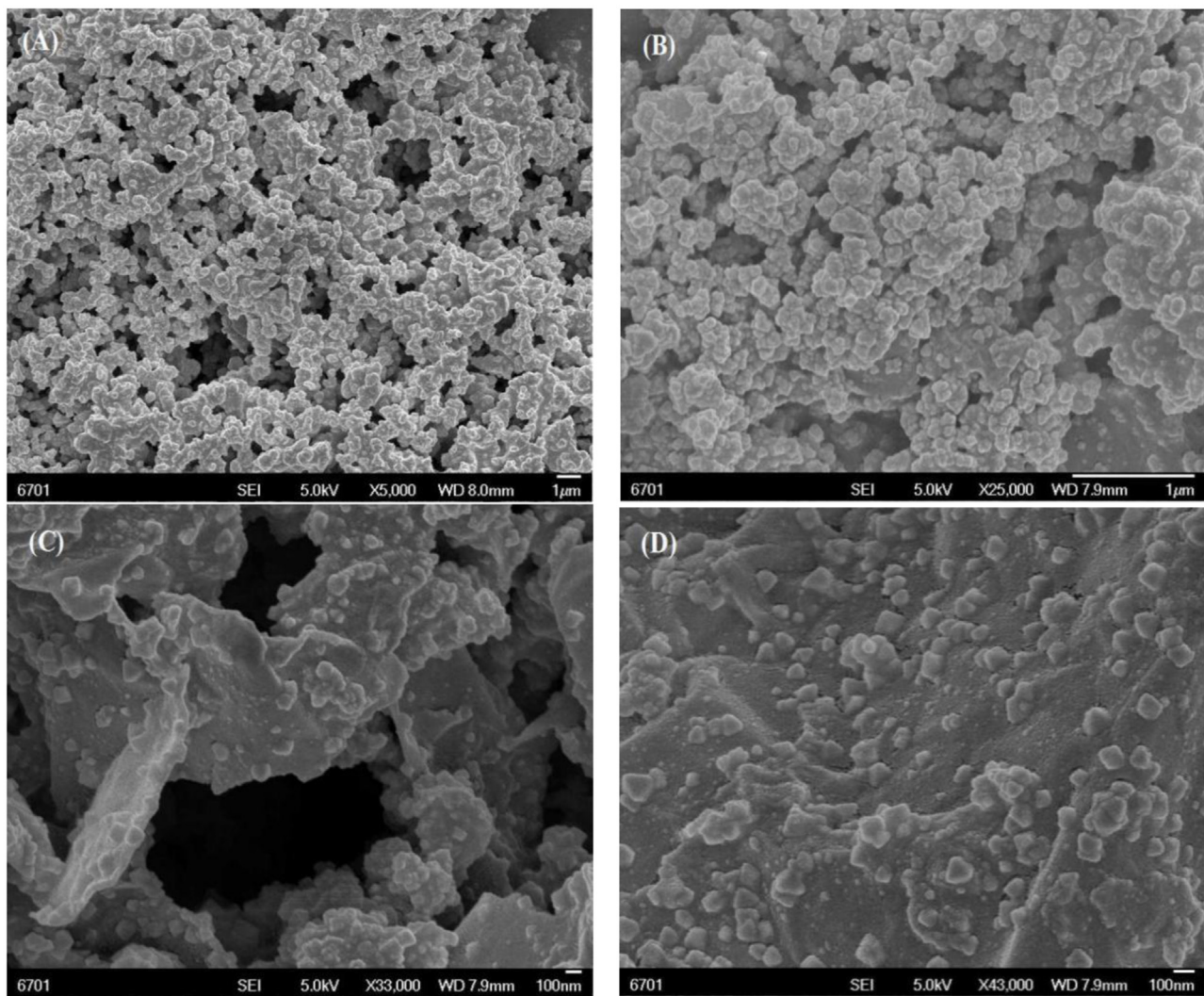


**Fig. 2.** SEM images of (A)  $\text{UiO-66-NH}_2$ ; (B)  $\text{UiO-66-NH}_2/\text{G}$ ; and (C–D) 5 wt%  $\text{MoS}_2$  QDs/ $\text{UiO-66-NH}_2/\text{G}$  composites.

can be observed. For the  $\text{MoS}_2$  QDs/G and  $\text{UiO-66-NH}_2/\text{G}$  samples, the peak belong to graphene is not observed. As for the sample of  $\text{MoS}_2$  QDs/ $\text{UiO-66-NH}_2/\text{G}$ , the peaks of  $\text{MoS}_2$  QDs and graphene is not appear, only the XRD pattern of  $\text{UiO-66-NH}_2$  is observed. The possible reason is that the content of  $\text{MoS}_2$  QDs too small to examine. It can be concluded that the  $\text{MoS}_2$  QDs and graphene have not destroyed the structure of  $\text{UiO-66-NH}_2$ .

### 3.1.2. SEM characterization

The morphologies of  $\text{UiO-66-NH}_2$ ,  $\text{UiO-66-NH}_2/\text{G}$  and  $\text{MoS}_2$  QDs/ $\text{UiO-66-NH}_2/\text{G}$  nanocomposites were examined by SEM. The pure  $\text{UiO-66-NH}_2$  (Fig. 2A) is prone to multi-stacking porous structures of irregular nanoparticles, many hollow structures can be observed on the surface. The  $\text{UiO-66-NH}_2/\text{G}$  (Fig. 2B) is also presented as the similar porous structure to the  $\text{UiO-66-NH}_2$ , but the irregular nanoparticles is more bigger. From Fig. 2C, it can be see that  $\text{UiO-66-NH}_2$  nanoparticles decorated on the surface of graphene sheets. The some rhombus-like and irregular particles are decorated on the surface of graphene sheets in the composite of  $\text{MoS}_2$  QDs/ $\text{UiO-66-NH}_2/\text{G}$  (Fig. 2D), and they appear to uniform distribution which have a diameter of 5–100 nm. Furthermore, the  $\text{MoS}_2$  QDs is not clearly observed on the surface of  $\text{UiO-66-NH}_2/\text{G}$ , it will further characterization by TEM.

### 3.1.3. TEM characterization

The TEM images of the  $\text{UiO-66-NH}_2/\text{G}$  nanocomposite revealed that a large amount of rhombus-like nanoparticles of  $\text{UiO-66-NH}_2$  grown on the surface of graphene sheets in Fig. 3A, which is agreement with the SEM images results of Fig. 2C and D. Fig. 3B and C clearly indicate that the increasing introduction of  $\text{MoS}_2$  QDs led to the agglomeration of  $\text{MoS}_2$  QDs on the surface of  $\text{UiO-66-NH}_2/\text{G}$  in the composite of  $\text{MoS}_2$  QDs/ $\text{UiO-66-NH}_2/\text{G}$ . The energy dispersive X-ray (EDX) results further confirm the co-existence of C, N, Zr, Mo and S elements in the area of red square of the  $\text{MoS}_2$  QDs/ $\text{UiO-66-NH}_2/\text{G}$  nanohybrid (Fig. 3D), which was supported by the XPS results of  $\text{MoS}_2$  QDs/ $\text{UiO-66-NH}_2/\text{G}$ .

### 3.1.4. X-ray photoelectron spectroscopy (XPS)

With a view to further ascertain the details of the chemical composition and elemental states of 5 wt%  $\text{MoS}_2$  QDs/ $\text{UiO-66-NH}_2/\text{G}$ , XPS measurements were carried out. The XPS survey spectrum, as presented in Fig. 4A, revealing that the catalyst mainly consist of Zr, C, N, Mo, S, and O elements, which in agreement with the EDX results. In Fig. 4B, the curve of Zr 3d region could be deconvoluted into two peaks for Zr  $3d_{5/2}$  and Zr  $3d_{3/2}$  located at around 182.20 eV and 184.70 eV, respectively [30]. In Fig. 4C, two single peaks at 395.14 eV and 399.68 eV can be observed for N 1s XPS spectrum. The former peak could be attributed to the N atoms of  $\text{NH}_2$  groups bonded with carbon atoms of graphene in the sample, whereas the

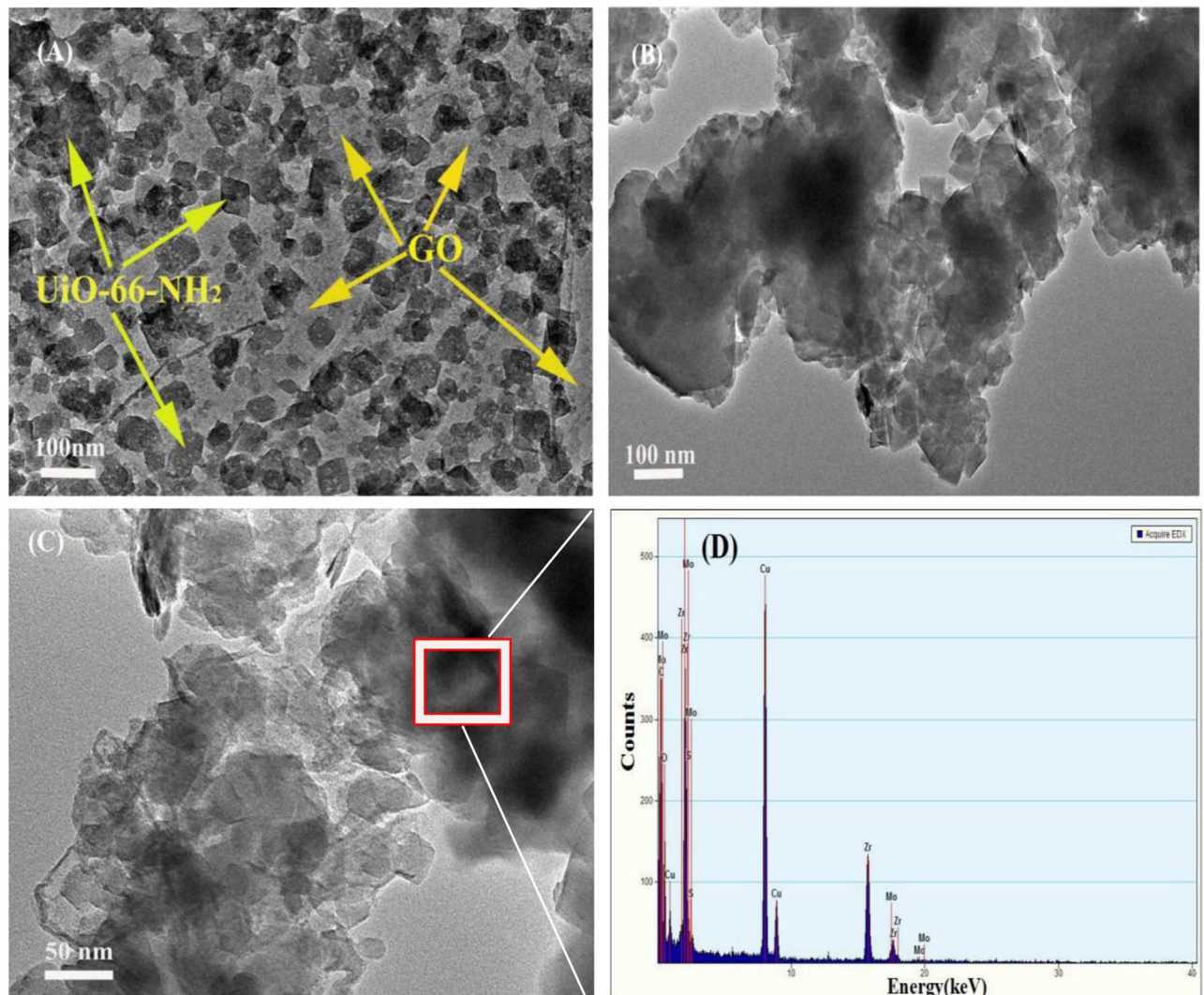


**Fig. 3.** TEM images of (A)  $\text{UiO-66-NH}_2/\text{G}$  and (B–C) 5 wt%  $\text{MoS}_2$  QDs/ $\text{UiO-66-NH}_2/\text{G}$  composites; (D) EDX spectrum of 5 wt%  $\text{MoS}_2$  QDs/ $\text{UiO-66-NH}_2/\text{G}$  in which the Cu signals originated from the Cu grid support for the TEM observation.

latter peak could be assigned to the retained organic linkers- $\text{NH}_2$  groups which do not bond with carbon atoms of graphene after the hydrothermal processing. In Fig. 4D, the C 1s can be deconvoluted into three peaks, the peak located at 284.85 can be assigned to carbon  $\text{sp}^2$  in phenyl for the catalyst or the amorphous. The peak at 286.58 eV could be attributed to the C–O in the graphene sheets, and the peak at 288.84 eV, which represent the C–N–H and C–N–C functional groups in the  $\text{MoS}_2$  QDs/ $\text{UiO-66-NH}_2/\text{G}$  structure. The Mo 3d spectrum in Fig. 4E shows the binding energy of Mo 3d<sub>3/2</sub> (232.43 eV) and Mo 3d<sub>5/2</sub> (229.2 eV) indicated that Mo was in the form of  $\text{Mo}^{4+}$  in  $\text{MoS}_2$  QDs. The peak at 235.62 eV is attributed to  $\text{Mo}^{6+}$  in  $\text{MoO}_3$ . In Fig. 4F, the peak at 162.06 eV is ascribed to S 2p<sub>3/2</sub>, while the peak at 163.23 eV could be assigned to S 2p<sub>1/2</sub>. The other peak at around 169.31 eV could be attributed to the  $\text{SO}_4^{2-}$  species, which maybe originate from the  $\text{MoS}_2$  during photocatalytic processing. Both the high resolution spectra of Mo 3d and S 2p ascertain the existence of  $\text{MoS}_2$  QDs in the composite.

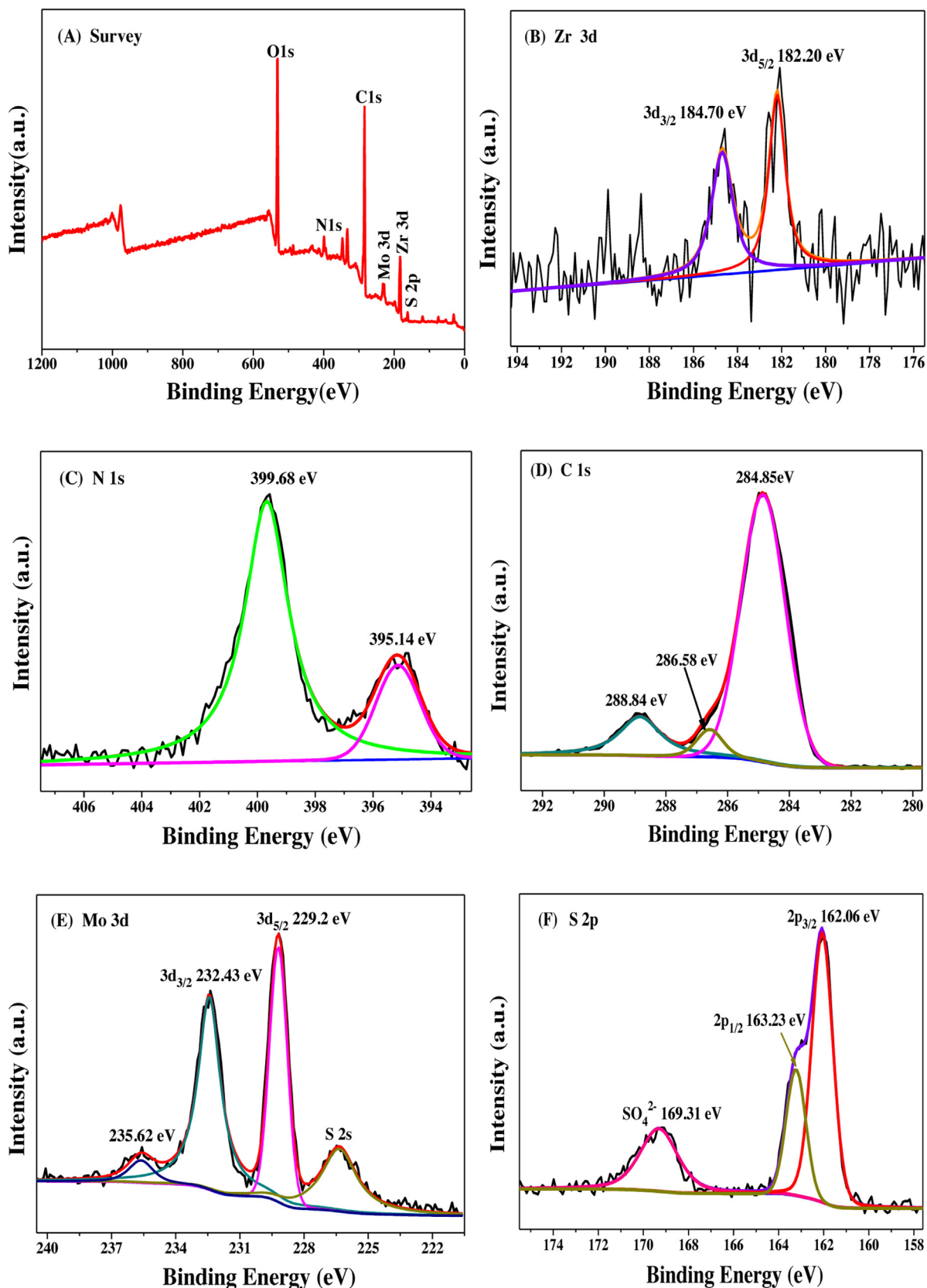
### 3.1.5. UV-vis diffuse reflectance spectra

The optical property of  $\text{MoS}_2$  QDs/ $\text{UiO-66-NH}_2/\text{G}$  composite was investigated using UV-vis diffuse reflectance spectroscopy. All the samples absorb UV to visible light as expected (Fig. 5), which signifies their visible-light-induced photocatalytic activity. The pure

$\text{UiO-66-NH}_2$  sample shows an absorption edge of  $\sim 435$  nm corresponding to a band gap of 2.78 eV. The absorption onset of the  $\text{MoS}_2$  QDs is at 461 nm, corresponding to a band gap of 1.69 eV. The excitonic peak at 660 nm deriving from the K point of the Brillouin zone of  $\text{MoS}_2$ , which can be distinctly observed both in the composites and in  $\text{MoS}_2$  QDs, revealing  $\text{MoS}_2$  QDs has been successfully decorated on the surface of  $\text{UiO-66-NH}_2/\text{G}$  [2]. Compared with pure  $\text{UiO-66-NH}_2$  and  $\text{MoS}_2$  QDs, the  $\text{MoS}_2$  QDs/ $\text{UiO-66-NH}_2/\text{G}$  composite shows a much stronger absorption within the visible light range and a red shift appears upon the addition of  $\text{MoS}_2$  QDs and graphene, as well as the intensity increases.

### 3.1.6. Brunauer–Emmett–Teller (BET) nitrogen adsorption isotherm characterization

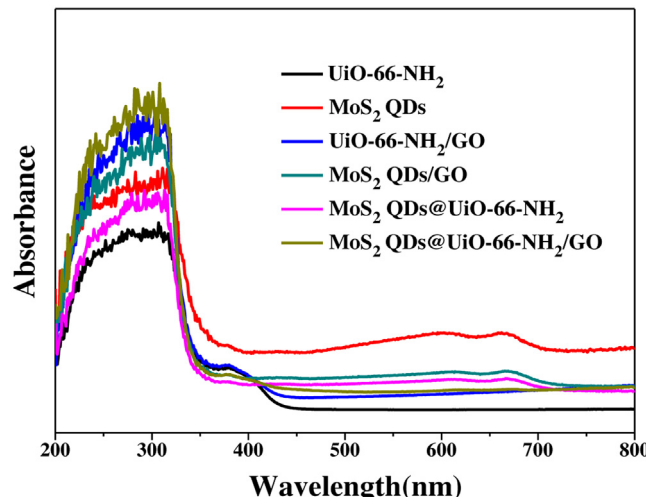
In order to analyze the textural properties of these samples, the BET surface area and the corresponding curves of the pore size distributions for the samples are investigated using nitrogen adsorption–desorption isotherms measurements at 77 K. The pore size distributions were determined using desorption data by the Barrett–Joyner–Halenda (BJH) method. For the  $\text{UiO-66-NH}_2$ ,  $\text{UiO-66-NH}_2/\text{G}$ ,  $\text{MoS}_2$  QDs/ $\text{UiO-66-NH}_2/\text{G}$  samples, the curves are type IV isotherms with H3 typical hysteresis loop, as observed in Fig. 6A. At the high relative pressure ( $P/P_0$ ) they show high



**Fig. 4.** XPS patterns of 5 wt% MoS<sub>2</sub> QDs/UiO-66-NH<sub>2</sub>/G sample. (A) Survey spectra, (B) Zr 3d, (C) N 1s, (D) C 1s, (E) Mo 3d and (F) S 2p scan spectra of the MoS<sub>2</sub> QDs/UiO-66-NH<sub>2</sub>/G sample.

**Table 1**Structural parameters obtained from  $N_2$  adsorption isotherms analysis.

Samples	$S_{BET}$ ( $m^2 g^{-1}$ ) <sup>a)</sup>	Pore volume ( $cm^3 g^{-1}$ ) <sup>b)</sup>	Average pore size (nm) <sup>b)</sup>
UiO-66-NH <sub>2</sub>	712.33	0.35	2.04
UiO-66-NH <sub>2</sub> /G	557.78	0.34	2.55
MoS <sub>2</sub> QDs/UiO-66-NH <sub>2</sub> /G	457.24	0.29	2.46

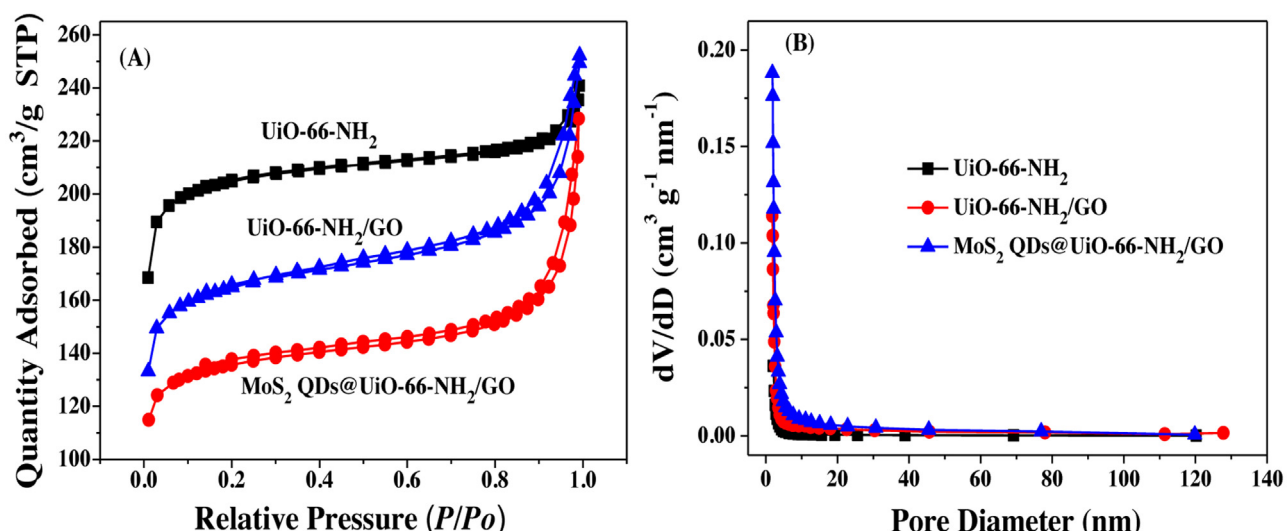
<sup>a)</sup>Obtained from BET method;<sup>b)</sup>Total pore volume taken from the  $N_2$  adsorption volume at a relative pressure ( $P/P_0$ ) of 0.97.**Fig. 5.** UV-vis diffuse reflectance spectra of UiO-66-NH<sub>2</sub>, MoS<sub>2</sub> QDs, UiO-66-NH<sub>2</sub>/G, MoS<sub>2</sub> QDs/G, MoS<sub>2</sub> QDs/UiO-66-NH<sub>2</sub>, MoS<sub>2</sub> QDs/UiO-66-NH<sub>2</sub>/G samples.

adsorption, indicating the presence of accumulative pores [20]. The  $S_{BET}$  of UiO-66-NH<sub>2</sub>, UiO-66-NH<sub>2</sub>/G, MoS<sub>2</sub> QDs/UiO-66-NH<sub>2</sub>/G were 712.33, 557.78 and 457.24  $m^2 g^{-1}$ , respectively. The  $S_{BET}$  of UiO-66-NH<sub>2</sub> sample (712.33  $m^2 g^{-1}$ ) gradually dwindle after add graphene (557.78  $m^2 g^{-1}$ ) and MoS<sub>2</sub> QDs (457.24  $m^2 g^{-1}$ ), which indicating graphene and MoS<sub>2</sub> QDs have a marked influence to the  $S_{BET}$  of samples. The pore size distributions curves in Fig. 6B show that porous UiO-66-NH<sub>2</sub>, UiO-66-NH<sub>2</sub>/G, MoS<sub>2</sub> QDs/UiO-66-NH<sub>2</sub>/G display a similar curves, which mainly consist of large size pores. For all of these samples show a mesoporous structure, which are confirmed by the corresponding pore size distribution as shown in Table 1. Meanwhile, Compared to the UiO-66-NH<sub>2</sub>/G, the MoS<sub>2</sub>

QDs/UiO-66-NH<sub>2</sub>/G has a smaller pore volume (0.29  $cm^3 g^{-1}$ ) and pore size (2.46 nm), which suggesting that the introduced MoS<sub>2</sub> QDs maybe get into to the porous structures and channels of MOF result in the reduce of pore volume and pore size. This is maybe more conducive to the catalytic reaction.

### 3.2. Photocatalytic activities over Eosin Y-sensitized MoS<sub>2</sub> QDs/UiO-66-NH<sub>2</sub>/G for H<sub>2</sub> evolution

The photocatalytic activities of the catalysts were evaluated using TEOA as sacrificial donor under visible light irradiation ( $\lambda \geq 420$  nm). As shown in Fig. 7, the presence of MoS<sub>2</sub> QDs and graphene were crucial for improving the photocatalytic H<sub>2</sub> evolution activity. The amount of H<sub>2</sub> over EY-sensitized UiO-66-NH<sub>2</sub> generated only 1.07  $\mu\text{mol}$  which increased a little after decorated on the graphene (1.98  $\mu\text{mol}$ ), suggesting that the UiO-66-NH<sub>2</sub> itself was inactive for H<sub>2</sub> evolution probably due to its cannot absorb visible light. For the MoS<sub>2</sub> QDs, there 37.62  $\mu\text{mol}$  H<sub>2</sub> was produced after 3 h irradiation. When introduction of the graphene, the photocatalytic activity reached 63.09  $\mu\text{mol}$ , which indicating the synergistic effect existence between MoS<sub>2</sub> QDs and graphene. Very interestingly, the H<sub>2</sub> evolution of MoS<sub>2</sub> QDs/UiO-66-NH<sub>2</sub> reached 75.1  $\mu\text{mol}$ , which was more active than the MoS<sub>2</sub> QDs/G. It was maybe existed the formation of the synergistic effect between MoS<sub>2</sub> QDs and UiO-66-NH<sub>2</sub> for hydrogen evolution. These results shown that MoS<sub>2</sub> QDs can as a photocatalyst and co-catalyst for photocatalytic H<sub>2</sub> production effectively under visible light. Thereby, for MoS<sub>2</sub> QDs/UiO-66-NH<sub>2</sub>/G, the H<sub>2</sub> generation rate reached 186.37  $\mu\text{mol}$ , which was significantly increased as expected, owing to the quantum confinement effect of MoS<sub>2</sub> QDs can help in the charge separation, and the synergistic effect of MoS<sub>2</sub> QDs and graphene together with UiO-66-NH<sub>2</sub> for electron transfer, thus enhancing the photocatalytic H<sub>2</sub> evolution activity. In this particular instance, MoS<sub>2</sub> QDs introduce active sites, graphene as electron

**Fig. 6.** (A) BET adsorption – desorption isotherms of catalysts and (B) the corresponding pore size distributions.

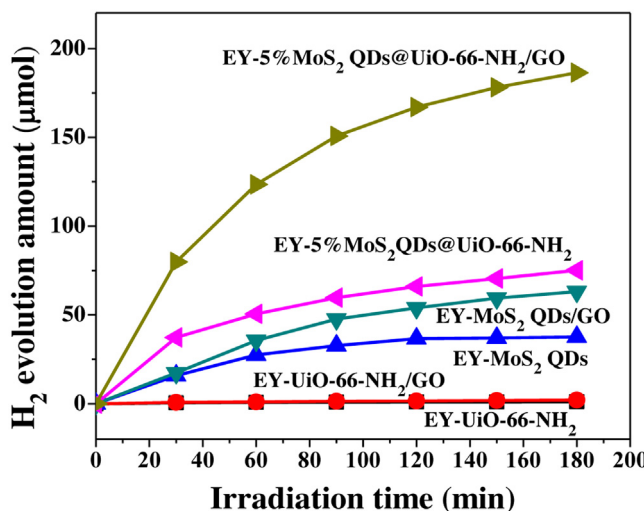


**Fig. 7.** The photocatalytic activities of the EY-sensitized ( $4.0 \times 10^{-4} \text{ mol L}^{-1}$ ) photocatalysts in 100 mL 10 v/v% TEOA aqueous solution (pH 7) for hydrogen evolution under visible light irradiation ( $\lambda \geq 420 \text{ nm}$ ).

transfer medium required for efficient  $\text{H}_2$  production in combination with the light absorbing unit, EY. The turnover number (TON) of dye Eosin Y for  $\text{H}_2$  evolution is calculated with the equation [2]. Here, the moles of dye Eosin Y is  $4 \times 10^{-5}$  in the reaction solution and the amount of production  $\text{H}_2$  is  $186.37 \mu\text{mol}$  in first 3 h over EY-5 wt%  $\text{MoS}_2$  QDs/UiO-66-NH<sub>2</sub>/G photocatalyst. Therefore, the calculated TON is 9.32 of dye Eosin Y in the first 3 h for photocatalytic  $\text{H}_2$  evolution.

### 3.3. Effect of the pH and the $\text{MoS}_2$ QDs ratio on the photocatalytic activity of $\text{MoS}_2$ QDs/UiO-66-NH<sub>2</sub>/G

It was known that the solution pH had a significant influence on photocatalytic activity [29]. As shown in Fig. 8A, acidic and strongly alkaline conditions are not conducive to  $\text{H}_2$  production. When pH values of TEOA aqueous solution varied from 5 to 9, the rate of photocatalytic hydrogen generation maximized at pH 7 ( $62.12 \mu\text{mol h}^{-1}$ ). The likely reason for the decrease rate of hydrogen evolution was that the state of TEOA which was affected by the pH of the solution. At acidic pH, more  $\text{H}^+$  results in protonation of TEOA, which was a less effective electron donor, thus leading to a shorter lifetime of the excited EY and lower efficiency of the excited dye species [28]. Under basic condition, the thermodynamic driving force for hydrogen evolution from water decreased due to the lower concentration of  $\text{H}^+$  [34]. Moreover, the adsorption behavior of EY onto the frameworks of UiO-66-NH<sub>2</sub> also be affected by the pH. The photocatalytic results indicated the dye can be effectively absorbed on the UiO-66-NH<sub>2</sub> at pH 7 and EY can be reductively quenched by TEOA absolutely at this pH 9.

In addition, we further investigated the influence of different content of  $\text{MoS}_2$  QDs loading to UiO-66-NH<sub>2</sub>/G on the photocatalytic hydrogen evolution activity, and a significant impact from the  $\text{MoS}_2$  QDs content was found. Fig. 8B emphasizes that the  $\text{MoS}_2$  QDs content is pivotal for optimal photocatalytic activity. At zero content, the UiO-66-NH<sub>2</sub>/G composite shown a tiny photocatalytic activity with a  $\text{H}_2$  generation rate of  $0.66 \mu\text{mol h}^{-1}$ . The photocatalytic hydrogen production increased with a rise in  $\text{MoS}_2$  QDs content. When a small amount of  $\text{MoS}_2$  QDs (1 wt %) introduced into the composite, the photocatalytic activity was enhanced to  $9.71 \mu\text{mol h}^{-1}$ , which is 14.5 times greater than that of the bare UiO-66-NH<sub>2</sub>/G. It is speculated that the quantum confinement effect of  $\text{MoS}_2$  QDs is beneficial to the charge separation and improve the photocatalytic activity as well. When the  $\text{MoS}_2$  QDs content

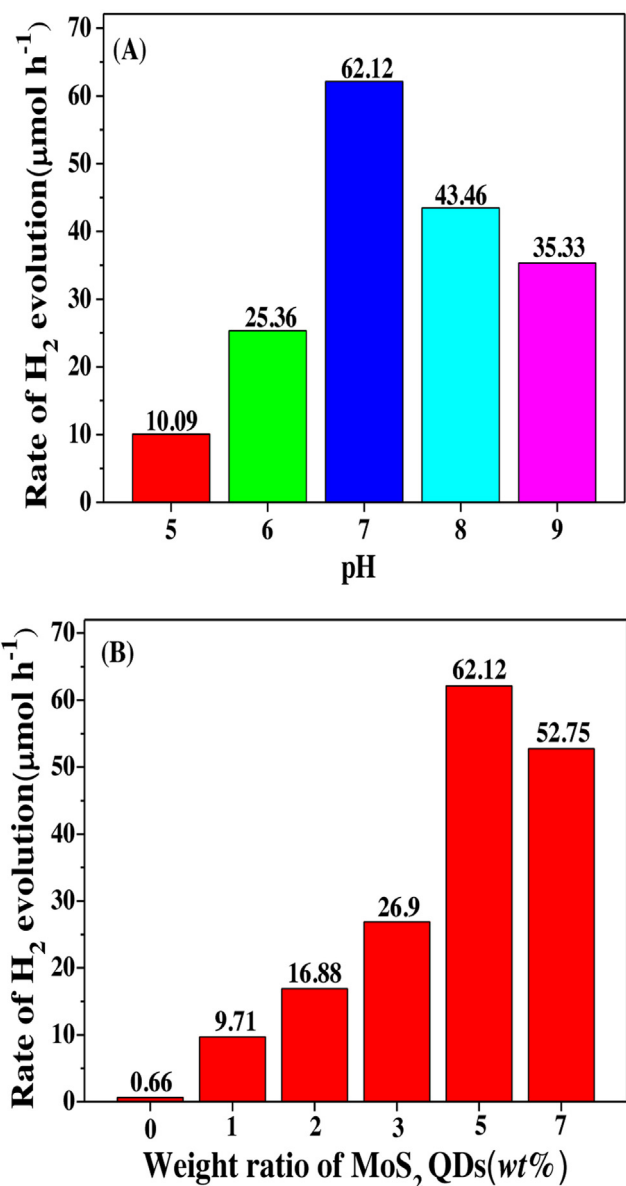


**Fig. 8.** (A) Effect of the pH on the photocatalytic activity of  $\text{MoS}_2$  QDs/UiO-66-NH<sub>2</sub>/G for hydrogen evolution and (B) effect of the different  $\text{MoS}_2$  QDs mass ratios from 1 to 7 on the photocatalytic activity of  $\text{MoS}_2$  QDs/UiO-66-NH<sub>2</sub>/G in 10% (v/v) TEOA aqueous solution (pH 7) under visible light irradiation.

up to 5 wt %, the  $\text{H}_2$  produced rate achieved a maximum value of  $62.12 \mu\text{mol h}^{-1}$ , which is 94.1 times higher than that of the UiO-66-NH<sub>2</sub>/G. Here, the turnover number (TON) of dye Eosin Y and  $\text{MoS}_2$  QDs for  $\text{H}_2$  evolution is 9.3 and 39.8 in the first 3 h, respectively. [Corresponding to an apparent quantum efficiency (AQE) of 40.5% at 430 nm]. And further increases in the  $\text{MoS}_2$  QDs content in the catalyst led to a downward photocatalytic activity. This maybe a higher  $\text{MoS}_2$  QDs content is agglomeration on the UiO-66-NH<sub>2</sub>/G that not in favor of the charge separation and the migration of photogenerated electrons.

### 3.4. Apparent quantum efficiencies (AQEs) and stability tests

The wavelength dependence of photocatalytic  $\text{H}_2$  evolution was investigated over a wide visible light range of 430–550 nm [32], and the apparent quantum efficiencies (AQEs) of EY sensitized 5 wt%  $\text{MoS}_2$  QDs/UiO-66-NH<sub>2</sub>/G for  $\text{H}_2$  evolution were calculated by the

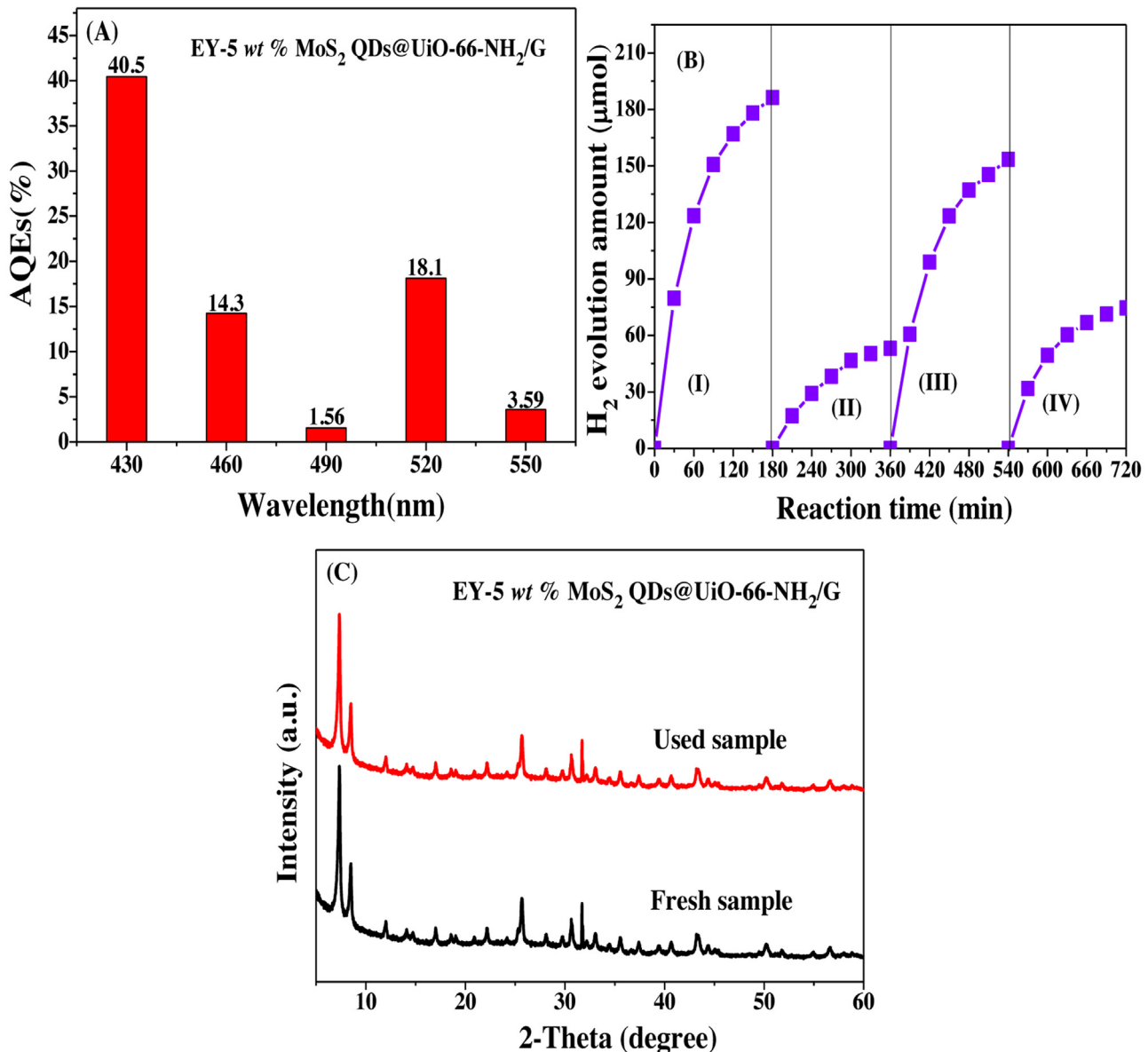


**Fig. 9.** Apparent quantum yields (AQEs) of hydrogen evolution for EY ( $4.0 \times 10^{-4}$  mol L<sup>-1</sup>) sensitized 5% MoS<sub>2</sub> QDs@UiO-66-NH<sub>2</sub>/G in 100 mL of 10 v/v% TEOA-H<sub>2</sub>O solution (pH 7) under different wavelength irradiation (reaction time: 30 min); (B) Stability test of EY sensitized 5 wt% MoS<sub>2</sub> QDs@UiO-66-NH<sub>2</sub>/G for H<sub>2</sub> generation under visible light irradiation in TEOA-H<sub>2</sub>O solution (pH 7). The reaction was continued for 720 min, with evacuation every 120 min. (I) First run; (II) evacuation; (III) add EY and TEOA, repeat II; (IV) repeat III. (C) The XRD patterns of before and after stability test of 5 wt % MoS<sub>2</sub> QDs@UiO-66-NH<sub>2</sub>/G.

corresponding formula. As shown in Fig. 9A, it can be observed that the AQEs decreases with increasing wavelengths and the highest AQEs was 40.5% at 430 nm. Interestingly, another high AQE was achieved at 520 nm, which was related to the highest absorption wavelength of EY (518 nm) [32]. These results suggested that the H<sub>2</sub> production reaction was indeed driven with the absorbing unit, EY.

The stability test of 5 wt% MoS<sub>2</sub> QDs@UiO-66-NH<sub>2</sub>/G was investigated over four runs of totally 720 min, and the results were shown in Fig. 9B. It was observed that in the first run, the maximum amounts of photocatalytic H<sub>2</sub> evolution was 186.37 μmol. But in the second run, the amounts of photocatalytic H<sub>2</sub> evolution sharply declined. The H<sub>2</sub> evolution activity of MoS<sub>2</sub> QDs@UiO-66-NH<sub>2</sub>/G could be revived by the concurrent addition of EY and TEOA in the third run. The reason is that the stability of the dye sensitizer is not good because of the adsorbed EY dye is easy to be desorbed and diffuse into the solution, and it could be decomposed

under light irradiation [25]. Whereas the XRD patterns of the fresh and used EY sensitized 5 wt% MoS<sub>2</sub> QDs@UiO-66-NH<sub>2</sub>/G (Fig. 9C) are almost the same, implying that MoS<sub>2</sub> QDs@UiO-66-NH<sub>2</sub>/G is stable under light irradiation.

### 3.5. Photoluminescence (PL) analysis

To prove the important role of MoS<sub>2</sub> QDs and graphene in facilitating the transfer of photogenerated electrons, the photoluminescence quenching of EY in the presence of the UiO-66-NH<sub>2</sub>, MoS<sub>2</sub> QDs, UiO-66-NH<sub>2</sub>/G, MoS<sub>2</sub> QDs/G, MoS<sub>2</sub> QDs@UiO-66-NH<sub>2</sub> and MoS<sub>2</sub> QDs@UiO-66-NH<sub>2</sub>/G were further performed. As shown in Fig. 10, EY solution ( $1 \times 10^{-6}$  mol L<sup>-1</sup>) excited at 480 nm shows a typically extensive emission peak at 539 nm. When the pure UiO-66-NH<sub>2</sub> was added, a slight decline occurred. As MoS<sub>2</sub> QDs, UiO-66-NH<sub>2</sub>/G, MoS<sub>2</sub> QDs/G, and MoS<sub>2</sub> QDs@UiO-66-NH<sub>2</sub> were introduced into the EY aqueous solution, a significant decrease was

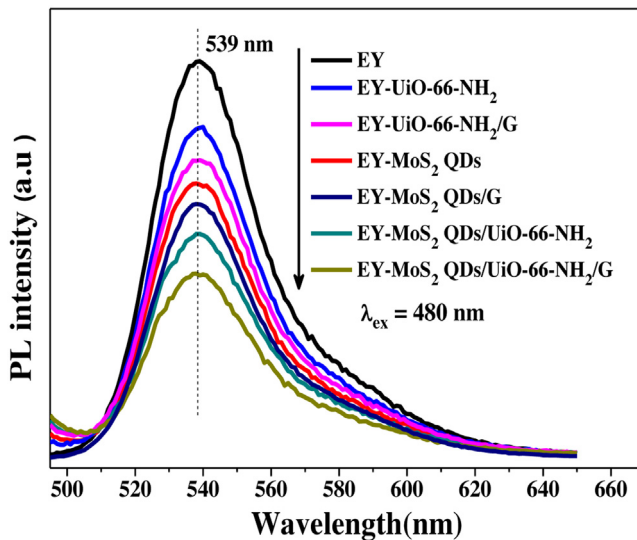


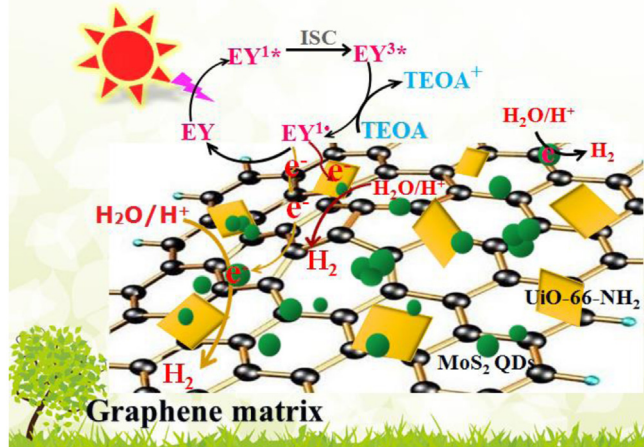
**Fig. 10.** Fluorescence spectra of the EY-sensitized  $\text{UiO-66-NH}_2$ ,  $\text{MoS}_2$  QDs,  $\text{UiO-66-NH}_2/\text{G}$ ,  $\text{MoS}_2/\text{G}$ ,  $\text{MoS}_2/\text{QDs}/\text{UiO-66-NH}_2$ ,  $\text{MoS}_2/\text{QDs}/\text{UiO-66-NH}_2/\text{G}$  in 10 v/v% TEOA aqueous solution at pH 7. [Catalysts]: 0.15 mg  $\text{mL}^{-1}$ .

observed at the emission wavelength of 539 nm, it can be attributed to graphene or  $\text{MoS}_2$  QDs which is believed to promote the migration of photo-generated electrons. And we can observed the photoluminescence dropped markedly when  $\text{MoS}_2$  QDs/ $\text{UiO-66-NH}_2/\text{G}$  was introduced, indicating formation the synergistic effect of  $\text{MoS}_2$  QDs and  $\text{UiO-66-NH}_2$  together with graphene, which is beneficial to the interfacial charge transfer and the separation efficiency of photogenerated electrons and holes in the  $\text{MoS}_2$  QDs/ $\text{UiO-66-NH}_2/\text{G}$  composites. The electron of excited dye molecule transfer to the catalyst surface when the dye adsorbed by offset face-to-face orientation *via*  $\pi$ - $\pi$  conjugation between EY and aromatic regions of the  $\text{UiO-66-NH}_2$  and graphene [33]. It is reasonable to assume that the electron transfers from excited dye to  $\text{UiO-66-NH}_2$  and graphene through the  $\pi$ - $\pi$  interactions, and finally electron transfers to  $\text{MoS}_2$  QDs [32]. This process efficiently improved the interfacial charge transfer and the separation efficiency of photo-generated charges, thus accounting for the  $\text{H}_2$  evolution activity significantly enhanced under visible light irradiation.

### 3.6. Electrochemical analysis

The charge transfer of the samples was studied by the Nyquist plots of electrochemical impedance spectroscopy (EIS) in dark. As shown in Fig. 11A, the semicircular diameter of EY- $\text{MoS}_2$  QDs/ $\text{UiO-66-NH}_2/\text{G}$  is the smallest compared with those of dye sensitized samples, indicating the excellent conductivity of the catalyst and further accelerated the charge transfer after introduction of  $\text{MoS}_2$  QDs and graphene. This phenomenon further proves the lower recombination rate of charges and fast interfacial electron transfer in EY- $\text{MoS}_2$  QDs/ $\text{UiO-66-NH}_2/\text{G}$  due to introduction of  $\text{MoS}_2$  QDs and graphene, which in agreement with the above PL results.

The transient photocurrent responses of dye sensitized  $\text{UiO-66-NH}_2$ ,  $\text{MoS}_2$  QDs,  $\text{UiO-66-NH}_2/\text{G}$ ,  $\text{MoS}_2/\text{G}$ ,  $\text{MoS}_2/\text{QDs}/\text{UiO-66-NH}_2$ ,  $\text{MoS}_2/\text{QDs}/\text{UiO-66-NH}_2/\text{G}$  coated on FTO was investigated for several on – off cycles of intermittent irradiation. As shown in Fig. 11B, The  $\text{MoS}_2$  QDs/ $\text{UiO-66-NH}_2/\text{G}$  composite shows the highest photocurrent intensity in the six samples, which is in accordance with the improved photocatalytic  $\text{H}_2$  evolution activity, whereas the lowest photocurrent intensity can be observed in the EY- $\text{UiO-66-NH}_2$  sample. The spectra results additionally reveals the photocatalytic activity of the composite can be attributed to the synergistic effect of  $\text{MoS}_2$  QDs and  $\text{UiO-66-NH}_2$  together with



**Scheme 1.** Photocatalytic mechanism for  $\text{H}_2$  production over EY sensitized  $\text{MoS}_2$  QDs/ $\text{UiO-66-NH}_2/\text{G}$  under visible light irradiation.

graphene, which greatly improved the interfacial electron transfer from EY to  $\text{MoS}_2$  QDs/ $\text{UiO-66-NH}_2/\text{G}$ . As a result, the photocatalytic  $\text{H}_2$  evolution activity was enhanced. Due to the dye Eosin Y is a miscible in aqueous solution, Eosin Y on the surface of FTO is dissolving in the electrolyte after a while, so lead to a higher dark current density over the high activity catalyst before measurement.

Furthermore, the electrochemical  $\text{H}_2$  evolution activities of dye sensitized  $\text{UiO-66-NH}_2$ ,  $\text{MoS}_2$  QDs,  $\text{UiO-66-NH}_2/\text{G}$ ,  $\text{MoS}_2/\text{G}$ ,  $\text{MoS}_2/\text{UiO-66-NH}_2$ ,  $\text{MoS}_2/\text{QDs}/\text{UiO-66-NH}_2/\text{G}$  electrodes were also investigated by the linear sweep voltammetry (LSV) technique. As shown in Fig. 11C, the cathodic current related to the reduction of water to  $\text{H}_2$  on bare FTO electrode was extremely low even at high applied potentials. But dye sensitized FTO/EY- $\text{UiO-66-NH}_2$ , FTO/ $\text{MoS}_2$  QDs, FTO/ $\text{UiO-66-NH}_2/\text{G}$ , FTO/ $\text{MoS}_2/\text{G}$ , FTO/ $\text{MoS}_2/\text{UiO-66-NH}_2$ , FTO/ $\text{MoS}_2/\text{QDs}/\text{UiO-66-NH}_2/\text{G}$  electrodes showed an increased cathodic current at a similar potential range and the highest current density was observed for the FTO/ $\text{MoS}_2/\text{QDs}/\text{UiO-66-NH}_2/\text{G}$  electrode, which clearly indicating  $\text{MoS}_2/\text{QDs}/\text{UiO-66-NH}_2/\text{G}$  material was a excellent electrocatalyst that could efficiently catalyze the reduction of water to  $\text{H}_2$ .

### 3.7. The speculation of mechanism for $\text{H}_2$ evolution

Based on the above characterizations, the reaction process of photocatalysis  $\text{H}_2$  evolution in EY-sensitized  $\text{MoS}_2$  QDs/ $\text{UiO-66-NH}_2/\text{G}$  system can be depicted in Scheme 1. The high photocatalytic  $\text{H}_2$  generation activity is attributed to the synergistic effect of the  $\text{MoS}_2$  QDs and graphene together with  $\text{UiO-66-NH}_2$ .  $\text{UiO-66-NH}_2$  has a large surface area of  $\sim 712.33 \text{ m}^2 \text{ g}^{-1}$ , well-ordered porous structures and channels, which is conducive to the dye absorption and electron transfer. When  $\text{UiO-66-NH}_2$  grown on the graphene, which creating most active-sites, like microreactor in the porous structures and channels of MOF on the surface of graphene.  $\text{MoS}_2$  QDs with much different exposed edges implanted on  $\text{UiO-66-NH}_2$  or graphene is conducive to the electron transfer owing to the quantum confinement effect of  $\text{MoS}_2$  QDs, which with graphene formation synergistic effect for electron transfer, thereby enhancing the photocatalytic  $\text{H}_2$  evolution activity. Under visible light irradiation, the absorbed EY on the surface of  $\text{UiO-66-NH}_2/\text{G}$  absorbs light photons to form singlet excited state  $\text{EY}^1*$ , which subsequently produces the lowest-lying triplet excited state  $\text{EY}^3*$  *via* an efficient intersystem crossing (ISC). Then,  $\text{EY}^3*$  is reductively quenched by TEOA to produce  $\text{EY}^{\bullet-}$  and oxidative donor ( $\text{TEOA}^+$ ) [29]. These  $\text{EY}^{\bullet-}$  species preferentially transferred to the  $\text{UiO-66-NH}_2$  and graphene, due to its electron transport characteristics, and then

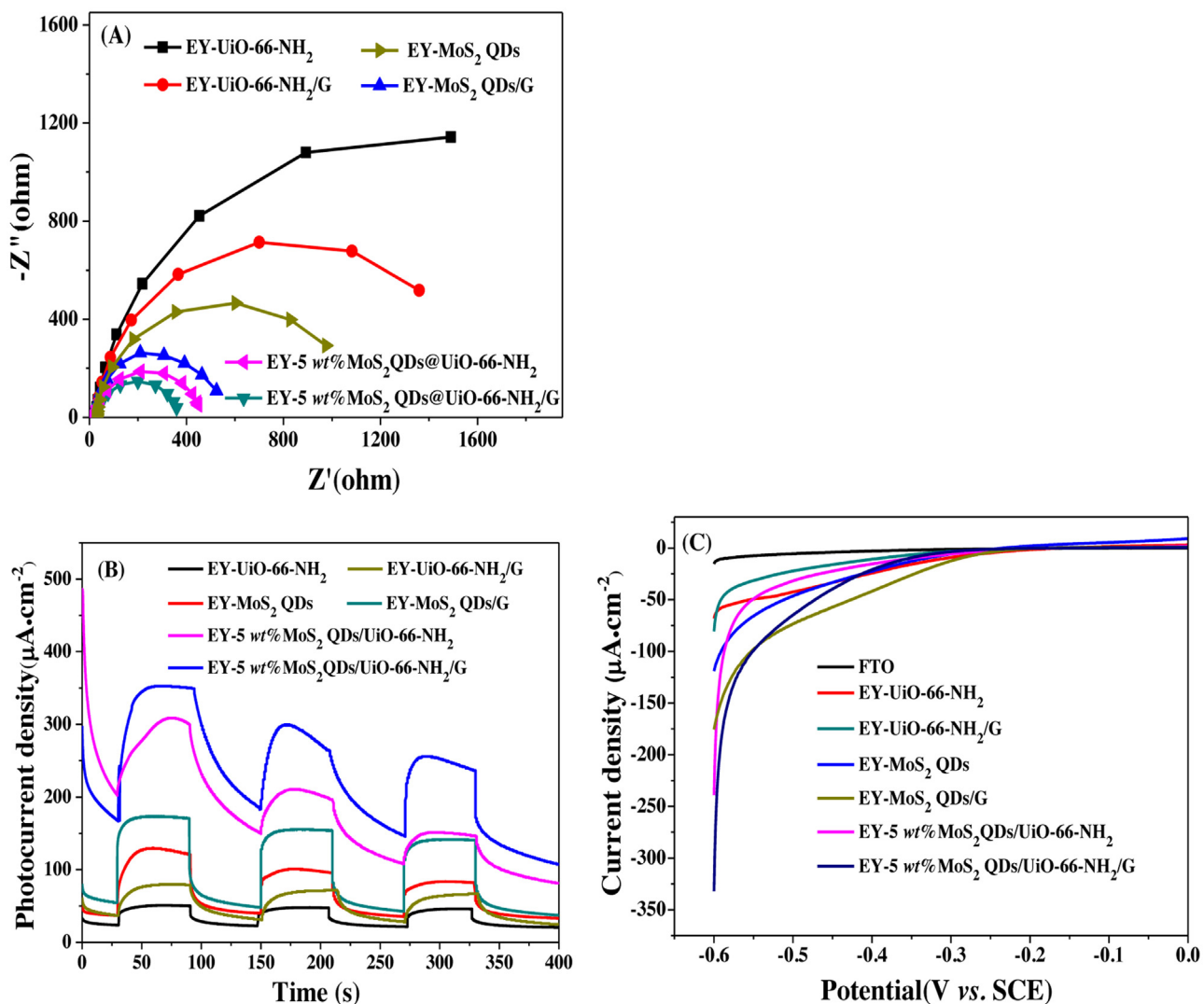


**Fig. 11.** (A) Nyquist plots of electrochemical impedance spectroscopy (EIS) and (B) transient photocurrent response for the EY-sensitized UiO-66-NH<sub>2</sub>, MoS<sub>2</sub> QDs, UiO-66-NH<sub>2</sub>/G, MoS<sub>2</sub> QDs/G, MoS<sub>2</sub> QDs/UiO-66-NH<sub>2</sub>, MoS<sub>2</sub> QDs/UiO-66-NH<sub>2</sub>/G coated on FTO in a mixed solution of 10 v/v% TEOA and Na<sub>2</sub>SO<sub>4</sub> (0.1 mol L<sup>-1</sup>) at pH 7 under visible light irradiation. (C) LSV curves of EY sensitized UiO-66-NH<sub>2</sub>, MoS<sub>2</sub> QDs, UiO-66-NH<sub>2</sub>/G, MoS<sub>2</sub> QDs/G, MoS<sub>2</sub> QDs/UiO-66-NH<sub>2</sub>, MoS<sub>2</sub> QDs/UiO-66-NH<sub>2</sub>/G coated on FTO in a mixed solution of 10 v/v% TEOA and Na<sub>2</sub>SO<sub>4</sub> (0.1 mol L<sup>-1</sup>) at pH 7. The scan rate was 1 mV s<sup>-1</sup>.

transferred to the loaded MoS<sub>2</sub> QDs where the protons are mainly reduced to form molecular H<sub>2</sub>. Simultaneously, the reduced state dye species get back to the ground state, accomplishing complete water reduction reaction. In addition, EY-sensitized MoS<sub>2</sub> QDs also can reduction H<sup>+</sup> to produce H<sub>2</sub>. UiO-66-NH<sub>2</sub> can function as an excellent dye adsorbent due to its porous structures and channel effect, and it can also act as an electron acceptor and transporter because of its channel confinement effect. Graphene also function as an excellent electron acceptor and transporter which with UiO-66-NH<sub>2</sub> synergistic efficiently prolong the lifetime of charge carriers and consequently improve the charge separation efficiency. Thus, the photocatalytic H<sub>2</sub> evolution activity of the MoS<sub>2</sub> QDs/UiO-66-NH<sub>2</sub>/G was remarkably enhanced. It is therefore concluded that the MoS<sub>2</sub> QDs have great potential to replace noble metal as cocatalyst for photocatalytic hydrogen evolution.

#### 4. Conclusions

In summary, a high active co-catalyst, MoS<sub>2</sub> QDs, anchored on UiO-66-NH<sub>2</sub>/G was employed as catalysts for the photocatalytic activity toward hydrogen evolution from water with Eosin Y as

antenna molecule under visible light irradiation. The introduction of MoS<sub>2</sub> QDs efficiently improved photo-generated charge carriers and electron transfer and significantly enhanced the photocatalytic hydrogen evolution. The UiO-66-NH<sub>2</sub>/G possessed high specific surface area (578.78 m<sup>2</sup> g<sup>-1</sup>) which supported MoS<sub>2</sub> QDs formation synergistic catalytic effect and exhibited the excellent photocatalytic activity and stability for hydrogen evolution. A possible reaction mechanism of the MoS<sub>2</sub> QDs/UiO-66-NH<sub>2</sub>/G was corroborated by photo-luminescence spectra, photo-electro-chemical characterizations and electro-chemical impedance spectra studies. Fluorescence studies shown that the charge separation and electrons transfer were more efficient by means of the introduction of MoS<sub>2</sub> QDs and graphene together with UiO-66-NH<sub>2</sub>. The UiO-66-NH<sub>2</sub>/G can not only contribute to the more efficiently absorb Eosin dye but also beneficial to efficiently transfer electrons due to the electron transport characteristics. Thus, the unusual catalytic activity arises from the synergistic effects between MoS<sub>2</sub> QDs and graphene together with UiO-66-NH<sub>2</sub>, and an excellent photocatalytic activity for H<sub>2</sub> evolution was obtained over the dye-sensitized MoS<sub>2</sub> QDs/UiO-66-NH<sub>2</sub>/G photocatalyst. The rate of H<sub>2</sub> evolution reached 62.12  $\mu\text{mol h}^{-1}$  over the EY-sensitized 5 wt%

MoS<sub>2</sub> QDs/UiO-66-NH<sub>2</sub>/G irradiated under visible light irradiation ( $\lambda \geq 420$  nm), and the apparent quantum efficiency (AQE) of 40.5% was achieved under 430 nm. MoS<sub>2</sub> QDs might be a promising alternative to replace noble-metal as cocatalyst for design new type of catalysts in photocatalysis proton reduction.

## Acknowledgement

This work was financially supported by the Chinese National Natural Science Foundation (21603274, 21263001, 41663012 and 21433007).

## References

- [1] F. Li, J. Li, Z. Cao, et al., *J. Mater. Chem. A* 3 (2015) 21772–21778.
- [2] X. Jin, X. Fan, J. Tian, et al., *RSC Adv.* 6 (2016) 52611–52619.
- [3] Y. Shi, B. Zhang, *Chem. Soc. Rev.* 45 (2016) 1529–1541.
- [4] W. Bi, L. Zhang, Z. Sun, et al., *ACS Catal.* 6 (2016) 4253–4257.
- [5] Q. Ye, H.B. Fang, Y.Z. Zheng, et al., *ACS Appl. Mater. Inter.* 8 (2016) 13879–13889.
- [6] U. Maitra, U. Gupta, M. De, et al., *Angew. Chem. Int. Ed.* 52 (2013) 13057–13061.
- [7] G. Gao, Y. Jiao, F. Ma, et al., *J. Phys. Chem. C* 119 (2015) 13124–13128.
- [8] P. Du, Y. Zhu, J. Zhang, et al., *RSC Adv.* 6 (2016) 74394–74399.
- [9] D. Escalera-López, Y. Niu, J. Yin, et al., *ACS Catal.* 6 (2016) 6008–6017.
- [10] X. Wang, G. Sun, N. Li, et al., *Chem. Soc. Rev.* 45 (2016) 2239–2262.
- [11] Z.X. Gan, L.Z. Liu, H.Y. Wu, et al., *Appl. Phys. Lett.* 106 (2015) 233113.
- [12] W. Gao, M. Wang, C. Ran, et al., *Chem. Comm.* 51 (2015) 1709–1712.
- [13] S. Xu, D. Li, P. Wu, *Adv. Funct. Mater.* 25 (2015) 1127–1136.
- [14] W. Qiao, S. Yan, X. Song, et al., *RSC Adv.* 5 (2015) 97696–97701.
- [15] X. Ren, L. Pang, Y. Zhang, et al., *J. Mater. Chem. A* 3 (2015) 10693–10697.
- [16] M. Alvaro, E. Carbonell, B. Ferrer, et al., *Chem. Eur. J.* 13 (2007) 5106–5112.
- [17] C. Wang, Z. Xie, K.E. deKrafft, et al., *J. Am. Chem. Soc.* 133 (2011) 13445–13454.
- [18] Y. Fu, D. Sun, Y. Chen, et al., *Angew. Chem.* 124 (2012) 3420–3423.
- [19] D. Sun, Y. Fu, W. Liu, et al., *Chem. A Eur. J.* 19 (2013) 14279–14285.
- [20] L. Shen, S. Liang, W. Wu, et al., *J. Mater. Chem. A* 1 (2013) 11473–11482.
- [21] C. Gomes Silva, I. Luz, F.X. Llabrés i Xamena, et al., *Chem. Eur. J.* 16 (2010) 11133–11138.
- [22] W.T. Xu, L. Ma, F. Ke, et al., *Dalton Trans.* 43 (2014) 3792–3798.
- [23] Y.P. Yuan, L.S. Yin, S.W. Cao, et al., *Appl. Catal. B: Environ.* 168 (2015) 572–576.
- [24] A. Fateeva, P.A. Chater, C.P. Ireland, et al., *Angew. Chem.* 124 (2012) 7558–7562.
- [25] J.J. Zhou, R. Wang, X.L. Liu, et al., *Appl. Surf. Sci.* 346 (2015) 278–283.
- [26] L. Shen, M. Luo, Y. Liu, et al., *Appl. Catal. B: Environ.* 166 (2015) 445–453.
- [27] J. He, J. Wang, Y. Chen, et al., *Chem. Comm.* 50 (2014) 7063–7066.
- [28] Q. Xiang, J. Yu, M. Jaroniec, *J. Am. Chem. Soc.* 134 (2012) 6575–6578.
- [29] X.Q. Hao, Z.L. Jin, G.X. Lu, et al., *Superlatt. Microstr.* 82 (2015) 599–611.
- [30] L. Shen, W. Wu, R. Liang, et al., *Nanoscale* 5 (2013) 9374–9382.
- [31] J.Y. Wu, X.Y. Zhang, X.D. Ma, et al., *RSC Adv.* 5 (2015) 95178–95182.
- [32] W. Zhen, J. Ma, G. Lu, *Appl. Catal. B: Environ.* 190 (2016) 12–25.
- [33] X. Zhang, L. Yu, R. Li, et al., *Catal. Sci. Technol.* 4 (2014) 3251–3260.
- [34] H. Zhang, X. Lv, Y. Li, Y. Wang, J. Li, *ACS Nano* 4 (2010) 380–386.